Journal of Alloys and Compounds 513 (2012) 404–413

Contents lists available at SciVerse ScienceDirect

Journal of Alloys and Compounds

journal homepage: www.elsevier.com/locate/jallcom

Electrical conductivity, dielectric properties and optical absorption of organic based nanocrystalline sodium copper chlorophyllin for photodiode application

A.A.M. Farag[a,*], A.M. Mansour[b], A.H. Ammar[a], M. Abdel Rafea[c], A.M. Farid[a]

[a] Thin Film Laboratory, Physics Department, Faculty of Education, Ain shams University, PO Box 11757, Roxy, Cairo, Egypt
[b] Solid State Electronics Laboratory, Physics Department, Physics Division, National Research Center, Dokki, Giza, Egypt
[c] Electronic Materials Department, Advanced Technologies and New Materials Institute, City for Scientific Research and Technology Applications, PO Box 21934, New Borg El-Arab City, Alexandria, Egypt

ARTICLE INFO

Article history:
Received 28 June 2011
Received in revised form 14 October 2011
Accepted 18 October 2011
Available online 25 October 2011

Keywords:
Organic semiconductor
Sodium copper chlorophyllin (SCC)
Electrical conductivity
Dielectric properties

ABSTRACT

Sodium copper chlorophyllin (SCC) thin films were successfully prepared, using dip coating technique. Thermal gravimetric analysis (TGA) was performed for studying the thermal stability of SCC film. The surface morphology of thin films was studied by using scanning electron microscopy (SEM). The crystalline structural characteristics were undertaken with the aim of determining the lattice parameters together with a complete list of the Miller indices and interplanar spacing for SCC. The molecular structure and electronic transitions of SCC were investigated by Fourier-transform infrared (FTIR) and absorption spectrum, respectively. Temperature dependence of the DC electrical conductivity, (σ_{DC}) was investigated in the temperature range 289–373 K. Measurements revealed that the σ_{DC} behavior of the films can be described by Mott's one-dimensional variable range hopping (VRH) model in the entire temperature range. The AC conductivity, ($\sigma_{AC}(\omega)$) results were discussed in terms of the correlated barrier hopping (CBH) mechanism for charge carrier transport. The maximum barrier height and the hopping length were estimated. The temperature dependence of the $\sigma_{AC}(\omega)$ shows Arrhenius type with one thermal activation energy for each frequency. The behavior of the real and imaginary parts of the dielectric constant as a function of both temperature and frequency were discussed. The energy band model was applied and the type of the optical transitions responsible for optical absorption was found to be direct allowed transition. Position dependent for SCC thin film photo-detector was studied by using laser diode source.

1. Introduction

In recent years, organic semiconductors represent an emerging class of electronic materials which have processing and performance advantages for large area utilization [1,2]. The remarkable combination of their novel semiconducting electronic properties with their ready shaping and manufacture makes them suitable for a wide range of applications ranging from flexible flat panel displays and smart cards to transistors, solar cells and even lasers [2,3]. Their attractive physical properties efficient electroluminescence, band gap in the infra-red (IR) to visible range, reasonable charge carrier mobility can be tuned by modifying their chemical structure [1]. There has been a wealth of activity directed at investigating the properties and structure of organic thin films [3,4]. Many researchers have been interested for using organic semiconductors thin layers in the electronics and optoelectronics applications [3–6]. This is mainly due to low cost, simplicity of fabrication of large areas, and their interesting optical and electronic properties [2–5]. In fact, stable and reproducible rectifiers have been successfully prepared in the field of electronic devices [3–6].

Chlorophyllin refers to any one of a group of closely related water-soluble salts that are semi-synthetic derivatives of chlorophyll, differing in the identity of the cations associated with the anion. Its most common form is a sodium/copper derivative used as a food additive and in alternative medicine [7].

The physical and chemical properties of these material layers depend not only on the molecular structure but also on the structure of the solid thin film [8,9]. One of the highly stable and water soluble derivatives of chlorophyll is the sodium copper chlorophyllin (SCC) which are formed by replacing the central magnesium atom by copper atom and then saponified by dissolving in ethanol containing NaOH.

The use of oxide films, i.e., TiO_2, ZnO, SnO_2 or Nb_2O_5 as a substrate to anchor the dye molecules such as chlorophyll and sodium copper chlorophyllin allows sunlight to be harvested over a broad spectral range in the visible region [10]. The mesoporous morphology of the oxides support plays a crucial role in the harvesting of sunlight. Similarly to chlorophyll in the green leaf, the dye acts as

* Corresponding author. Tel.: +20 2 33518705; fax: +20 2 22581243.
E-mail address: alaafaragg@yahoo.com (A.A.M. Farag).

0925-8388/$ – see front matter © 2011 Elsevier B.V. All rights reserved.
doi:10.1016/j.jallcom.2011.10.058

an electron transfer sensitizer. Upon excitation by light it injects electrons in the conduction band of the oxide resulting in separation of positive and negative charges. For efficient photoconversion of solar energy, the charge injection must occur with unit quantum yield [10].

A great advantage of dye-sensitized cells is that they can be used to produce directly high-energy chemicals from sunlight. Such "photosynthetic" devices solve the principal problem of conventional photovoltaic cells that is the lack of capacity for energy storage.

The choice of SCC for this study was motivated by the thermal and chemical stability as well as easily preparation process as a thin film by different methods such as spray and spin coating techniques [11,12]. In this work, the dip coating deposition method is used as a one of the cheapest methods to deposit thin films and nanomaterials, as it does not depend on expensive equipment and is a scalable technique that can be employed for large area batch processing or continuous deposition [13]. Up to our knowledge, there is no intensive results found in the literature concerning the carrier transport mechanisms and photovoltaic properties of SCC based devices except our publications of the UV–vis absorption studies [11] and the photovoltaic characteristics of SCC/*n*-Si heterojunction prepared by spray technique [12]. As an extension for these studies, the present work deals with the investigation of the structural, DC and AC electrical conductivities as well as photodiode applications of the prepared SCC by dip coating technique. Moreover, the temperature and frequency dependences of the electrical conductivity and the dielectric constants were also investigated. The analysis was done to determine some related parameters and predict the electronic conduction mechanisms of SCC film.

2. Experimental

2.1. Materials

Sodium copper chorophyllin (SCC) powder of purity 99.64% was used in the present study. Pure gold and aluminum electrodes were used as ohmic and blocking contacts, respectively with SCC. The molecular structure of SCC is shown in Fig. 1(a).

2.2. Thin film preparation

Thin films of SCC were prepared by dip coating technique, using chloroform as a solvent under stirring condition at temperature close to 323 K for dip-coating process. Stirring continued for more 1 h to ensure the homogeneity of the mixture. The glass square (2.5 cm × 2.5 cm) substrates used in this study were cleaned successively with distilled water, acetone and ethanol. After which it dried with an air gun. A solution contained 0.2 mol L^{-1} of SCC was prepared using chloroform as a solvent. Many factors contribute to determine the final state of a dip coated thin film were controlled such as the initial substrate surface (≈2.5 cm × 2.5 cm), substrate temperature (≈303 K), solution temperature (≈323 K), submersion time (≈10–15 s), withdrawal speed (≈20–40 mm/s), and environment humidity (≈70%). A large variety of repeatable dip coated film structures and thicknesses can be fabricated. The set-up of the used dip coating technique shown in Fig. 1(b) can give uniform; high quality film using DC motor control of the dipping arm provides smooth linear motion of the substrate at all dipping speeds. A variety of speed ranges are available with the possibility of slow speed. After preparation the films coated on the substrates were dried in electric oven at 350 K to evaporate the residual solvent. The prepared films of SCC are nearly homogeneous and uniform allover glass sides. The thickness of the prepared film is approximately ≈2–3 μm.

2.3. Methods and characterization tools

Thermal gravimetric analysis, TGA (Shimadzu TGA-50, Japan) was carried out for the SCC in order to study their thermal stability. TGA curve was obtained by heating approximately 10 mg SCC powder from 20 to 600 °C at a heating rate of 10 °C/min in a flow rate of 20 ml min^{-1} pure nitrogen atmosphere to avoid thermal oxidation. Furnace control employed algorithms enabling closely occurring decomposition events to be separated. Thermal decomposition profiles were used to interpret and compare thermal stability.

A Philips model X'pert diffractometer with CuK_α radiation operated at 40 kV and 25 mA was used for the structural investigation of SCC film.

The surface topography of SCC film was imaged, using a scanning electron microscopy, SEM (JEOL JSM 6360LA, Japan) operated at 25 kV, with resolution power of 4 nm. The SCC films were prepared by coating with ~50 nm of sputtered gold.

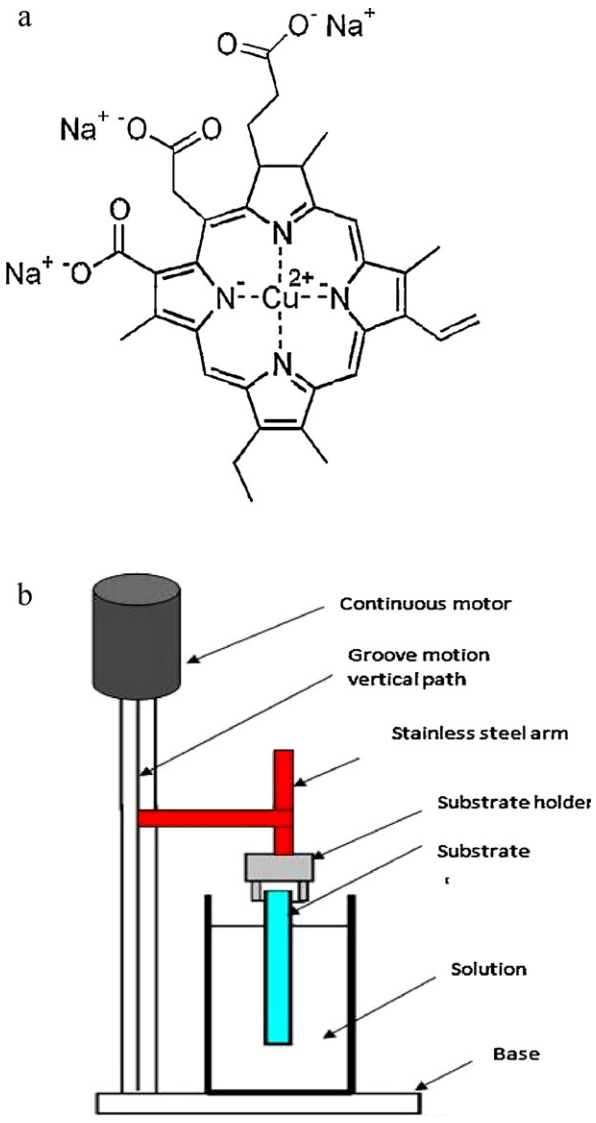

Fig. 1. (a) Structural formula of SCC. (b) Set-up of dip coating process.

The infrared absorption spectrum of the prepared SCC film were measured at room temperature in the range (4000–400) cm^{-1} by an infrared spectrophotometer (Shimadzu 8400S, Japan) using the KBr disc technique. The KBr disc was subjected to a load of 5 tons cm^{-2} for 2 min to produce clear homogenous disc. The IR absorption spectrum was measured immediately after preparing the disc.

The two-point probe technique was used for electrical measurements for SCC thin films with a thickness of ~500 nm. The measurement of the dark DC electrical conductivity of SCC films was carried out in the temperature range from 289 to 373 K, using a high impedance electrometer (Keithley 617 A). The temperature was measured directly by Type-K thermocouple connected to the temperature controller (Eurotherm model no. 390-200) to avoid the sudden drop in the heater temperature using a closed furnace under air conditions.

The measurements of the AC electrical conductivity of SCC films were measured using programmable automatic LCR Bridge (model Hioki 3532 Hitester). The measurements were carried out on the parallel circuit mode. The measurements were performed in the temperature range 300–375 K and frequency ranges 100 kHz–1 MHz.

3. Results and discussion

3.1. Thermal analysis

The SCC film was studied and evaluated by using thermal gravimetric analysis (TGA) [14–16] in order to confirm the possible thermal stability characteristics the SCC molecule. The results of the TGA are compiled in Table 1 as the decomposition steps, mass and

Table 1
TGA extracted data of SCC film.

Degradation step	Temp. range (°C)	Mass loss (mg)	Percentage loss%
1st	50.6–106.4	0.114	1.70
2nd	227.5–391	1.35	20.15
3rd	392–592	0.37	5.52
Overall		1.834	27.31

percentage losses as well as decomposition temperature range. The TGA thermogram of SCC is shown in Fig. 2 and characterized by the presence of three discrete characteristic decomposition steps. The first decomposition step in SCC was identified in the temperature range of 50.6–106.4 °C with a percentage loss of 1.70%. This decomposition step may be related to volatilization of small molecule, and/or the evaporation of residual adsorbed water [14]. Sun [15] reported that the first loss of the mass due to chlorophyll degradation as a result of the dehydration of the tightly bound water of hydration. Seoudi et al. [16] showed that the first degradation in the TGA analysis may be due to the loss of moisture.

The second step in the temperature range of 227.5–391 °C is the major thermal decomposition step in SCC molecule with a percentage loss of 20.15%. This decomposition step may be correlated to the elimination of the Cu^{II} ion. The last decomposition step in the TGA of SCC required a wide temperature range for complete the degradation of the porphyrin structure (392–592 °C) and this decomposition step was found to correspond to a percentage loss of 5.52%. The overall percentage loss of the SCC molecule corresponds to 27.31% up to the maximum heating temperature (600 °C) specified by TGA conditions.

3.2. Morphological and crystalline structure of SCC film

Fig. 3 shows the surface morphology of a nanocrystalline SCC film using scanning electron microscope. The fine feature such as extremely small grain size of the film surface was observed. The average grain size was found to be about 44 nm. The particle size distribution of SCC film was recorded using particle size analyzer (PSA) which shows the average grain size of about 41 nm as shown in Fig. 4. The obtained particle size is found to be in agreement with that obtained by SEM.

The crystalline structural characteristics were undertaken with the aim of determining the lattice parameters together with a complete list of the Miller indices (*hkl*) and interplanar spacing (d_{hkl}) for SCC. The X-ray diffraction patterns (XRD) of the SCC thin film deposited by dip coating is shown in Fig. 5 and reveals

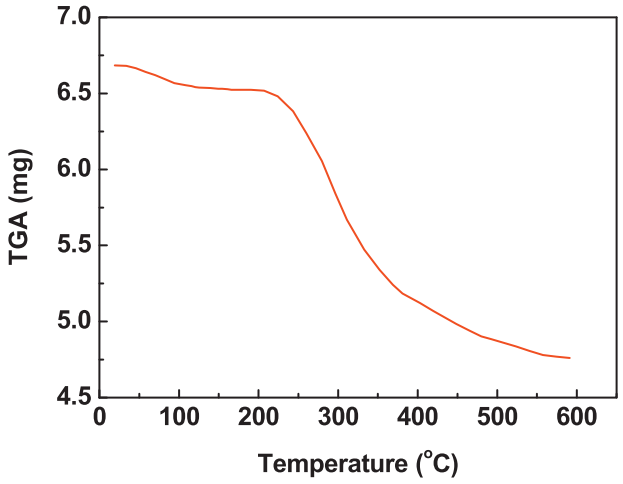

Fig. 2. Thermal gravimetric analysis (TGA) of SCC film.

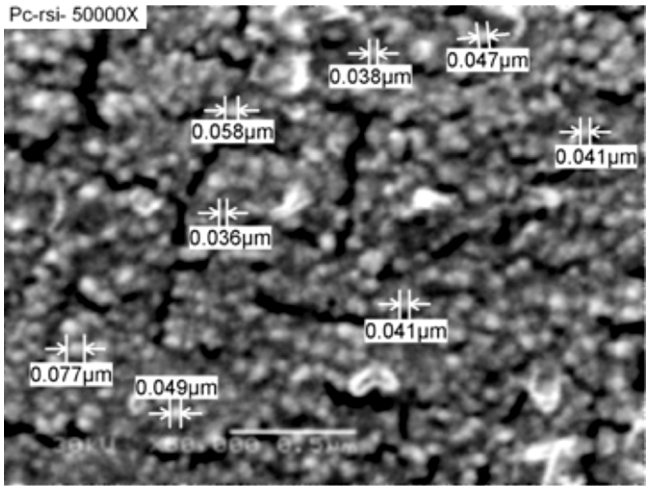

Fig. 3. Scanning electron microscopy (SEM) image of SCC film with magnification of 50,000× and scale of 500 nm (0.5 µm).

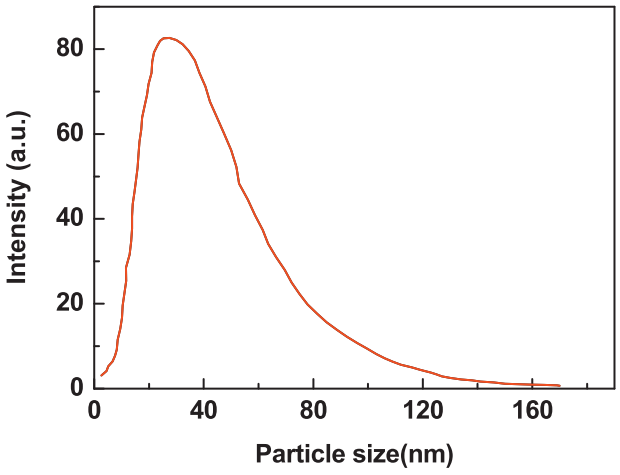

Fig. 4. Particle size analysis using analyzer, PSA of SCC film.

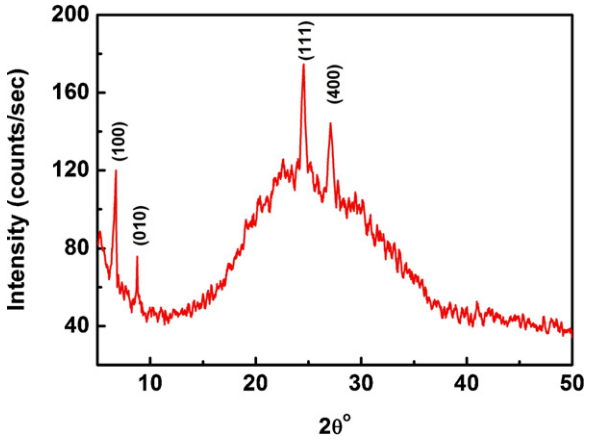

Fig. 5. X-ray diffraction (XRD) of SCC film.

nanocrystalline nature for the deposited film. The CRYSFIRE computer program [17] was applied for indexing all the obtained diffraction lines of the XRD of the powder SCC (not shown here). It was found that the difference between the calculated d_{hkl} values are in satisfactory agree with that observed by XRD as listed in Table 2. Therefore, the present deduced indexing can be accepted

Table 2
The observed and calculated interplanar spacing $d_{obs.}$ and the Miller indices (*hkl*) for powder SCC.

2θ (°)	$d_{obs.}$ (Å)	d_{hkl} (Å)	*hkl*
6.714	15.291	15.287	(1 0 0)
8.884	11.567	11.557	(0 1 0)
11.143	9.220	9.219	(1 1 0)
13.45	7.653	7.643	(2 0 0)
16.142	6.275	6.375	(2 1 0)
17.822	5.780	5.779	(0 2 0)
19.063	5.407	5.405	(1 2 0)
20.234	5.098	5.096	(3 0 0)
22.136	4.665	4.663	(3 1 0)
22.394	4.64	4.61	(2 2 0)
22.823	4.526	4.524	(1 0 1)
23.57	4.386	4.383	(0 1 1)
24.534	4.313	4.213	(1 1 1)
25.692	4.031	4.026	(2 0 1)
26.87	3.854	3.852	(0 3 0)
27.089	3.810	3.822	(3 2 0)
27.09	3.832	3.820	(4 0 0)
27.234	3.805	3.802	(2 1 1)
27.727	3.726	3.736	(1 3 0)
28.287	3.673	3.663	(0 2 1)
28.563	3.631	3.628	(4 1 0)
29.106	3.565	3.562	(1 2 1)
29.905	3.472	3.469	(3 0 1)

and the SCC lattice is orthorhombic crystallographic system with space group $P222_1$, with the lattice parameters: $a = 15.28693$ Å, $b = 11.5574$ Å, $c = 4.73629$ Å. The values of Miller indices, *hkl*, for each diffracted peak together with the interplanar spacing (d_{hkl}) were obtained by using CHECKCELL program [18] and listed in Table 2. On the other hand, the structure of the obtained SCC film is shown in Fig. 5. The diffracted peaks were oriented along the (1 0 0), (0 1 0), (1 1 1) and (4 0 0) directions. These clearly indicate that the prepared film has the same structure of the powder SCC film with orthorhombic crystallographic system. It is known that X-ray diffraction line broadening is influenced by the crystallite size and the internal strains. In order to obtain these parameters, Williamson-Hall method was used. In this method, the analysis includes two steps: first step, the width (β_{measured}) of every peak was measured as the integral breadth. The instrumental broadening ($\beta_{\text{instrument}}$) was determined from polycrystalline silicon standard.

Generally, the X-ray diffraction peak broadening is due to the instrumental broadening that due to crystallite size and lattice strain present in the material. The contributions of each of these effects are convoluted causing an overall broadening of the diffraction peaks. Before estimating the crystallite size and lattice strain, it is necessary to eliminate the instrumental effect. The instrumental corrected broadening β corresponding to the diffraction peak of SCC was estimated using the following equation [13]

$$\beta = \sqrt{\beta^2_{measured} - \beta^2_{instrumental}}, \quad (1)$$

where $\beta_{measured}$ and $\beta_{instrumental}$ are the full widths at half maxima (FWHM) of the broadened peaks of the SCC and a silicon crystal free from defect (standard), respectively. The use of silicon crystal free from defects enables to determine the instrumental broadening. The crystallite size (D) and lattice strain (ε) can be calculated using Williamson-Hall equation as follows [13]:

$$\beta \cos\theta = 4\varepsilon \sin\theta + \frac{K\lambda}{D}, \quad (2)$$

where λ is the X-ray wavelength of CuK_α (1.5418 Å) and K is the Scherrer's constant of the order of unity (0.9). Plotting of $\beta\cos\theta$ vs. $\sin\theta$ (shown in Fig. 6) produces a fit straight line of slope ($\approx 4\varepsilon$) and intercept ($\approx K\lambda/D$) in which the lattice strain and crystallite size are determined. The values of lattice strain and crystallite size were found to be 0.239 and 13.28 nm, respectively. The crystallite size obtained by XRD was found to be lower than that obtained by SEM and PSA.

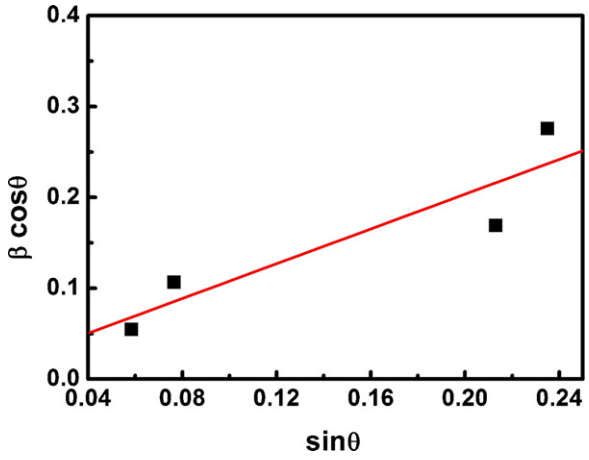

Fig. 6. Plot of $\varepsilon\cos\theta$ vs. $\sin\theta$ for SCC film.

3.3. IR absorption characteristics of SCC film

The infrared spectrum is the unique characteristic of functional groups stacking the molecule and is found to be the most useful physical method of investigation in identifying functional groups and to know the molecular structure. The absorption of IR radiation causes the various bands in a molecule to stretch and bend with respect to one another [19]. The most important range (400–4000) cm^{-1} is of prime importance for the study of an organic compound by spectral analysis [20]. The infrared spectrum has two regions. The fingerprint region is unique for a molecule and the functional group region is similar for molecules with the same functional groups [19]. For the ensuing discussion, this IR spectrum, shown in Fig. 7, is divided into four regions: (4000–2700), (1800–1600), (1600–1300) and (1300–400) cm^{-1} (the film of SCC is transparent in the region (2700–1800) cm^{-1}).

Absorption bands found in the high-frequency region of spectrum (4000–2700) cm^{-1}, shown in Fig. 7, are usually associated with O–H, N–H, and C–H stretching modes [4]. The broad intensity band at 3421.13 cm^{-1} can be logically assigned to an O–H stretching vibration of water. Adventitious water can arise from traces

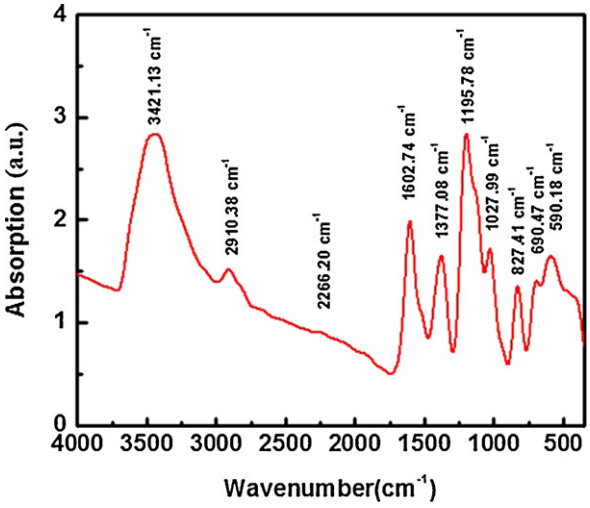

Fig. 7. Fourier-transform infrared, FTIR-absorption spectrum of SCC film.

Table 3
DC electrical conductivity data of SCC film.

	ΔE (eV)	T_0 (K)	ΔW (meV)	$\langle R \rangle$ (nm)
Present work	0.24	1.72×10^4	98	0.75
Pisharady Sreejith et al. [30]	0.30	6.42×10^3	57	0.11
Koval et al. [36]	–	10^4	–	0.35
Farag et al. [37]	–	5.8×10^4	–	–

of water in the potassium bromide. The 2910.38 cm^{-1} absorption is assigned to an asymmetric C–H stretching mode [22]. The absorption bands found in the region (1750–1600) cm^{-1} shows one absorption band at 1602.74 cm^{-1} which can be assigned to the carboxylate anion stretching [23].

The medium intensity absorption peaks that appear in the region (1600–1300) cm^{-1} most likely arise from the skeletal vibrations of the tetrapyrrolic macrocycle of the alkyl substituent of the porphyrin ring. The spectrum of the SCC film shows bands at 1377.08 cm^{-1} that may be assigned to the C=C and C=N skeletal vibrations of the porphyrin ring. Similar absorption bands in this general region of porphyrin [11,24] have previously been assigned in the same way.

The region below 1300 cm^{-1} is commonly known as the fingerprint region, even though it does include some stretching vibrations. The absorption in the region (1300–650) cm^{-1} is generally associated with molecular motions involving many atoms such as in and out-of-plane bending and breathing vibrations of ring structures. The spectrum of SCC in the fingerprint region is complex, and only tentative assignments of the absorption bands can be made. The 1195.78 cm^{-1} peak can be assigned to C–C stretching and bending in pyrrole ring and the absorption peak at 1027 cm^{-1} has been previously assigned to a pyrrole ring breathing mode [25]. The vinyl C–H out-of-plane bending mode absorbs at 827.41 cm^{-1}. One medium intensity band at 690.47 cm^{-1} and 590.18 cm^{-1} appear to be consistent with the metal legend (M–N) vibration band observed at high frequencies in the range (700–600) cm^{-1} for the Fe, CO, Ni, Cu, Zn, Pd, and Pt series of porphyrins based structure, indicating the extraordinary stability of SCC due to strong bonding between the metal ion and the four surrounding nitrogen atoms in the pyrrole rings [11,21–26].

3.4. DC electrical characteristics of SCC

Fig. 8(a) shows the temperature dependence of the dark DC conductivity, σ_{DC}, in the temperature range 289–373 K. DC conductivity, σ_{DC}, is gradually increasing with temperature in the measured temperature range. The increase in the conductivity as a function of temperature in a semilogarithmic plot signifies that the examined film exhibits semiconducting behavior. Fig. 8(b) shows the semilogarithmic plot of DC conductivity, σ_{DC}, of SCC as a function of reciprocal temperature. The well-defined straight line obtained from the Arrhenius plot suggests the presence of only one conduction mechanism in the temperature range of 289–373 K for the film. Thus, it is reasonable to represent the temperature dependence of σ_{DC} for the film by the well-known expression [27–29],

$$\sigma_{DC}(T) = \sigma_0 \exp\left(-\frac{\Delta E}{kT}\right), \quad (3)$$

where σ_0 is the conductivity at infinite temperature, ΔE is the activation energy and k is the Boltzmann's constant. The value of ΔE derived from the slope of the $\log \sigma_{DC}$ versus $1/T$ graph, respectively was determined and listed in Table 3. The obtained value of ΔE is in agreement with that obtained by Pisharady Sreejith et al. [30].

The temperature dependence of conductivity is originating from quasi one-, two- or three-dimensional variable range hopping (VRH) across the barriers [31,32] or at very low temperatures VRH

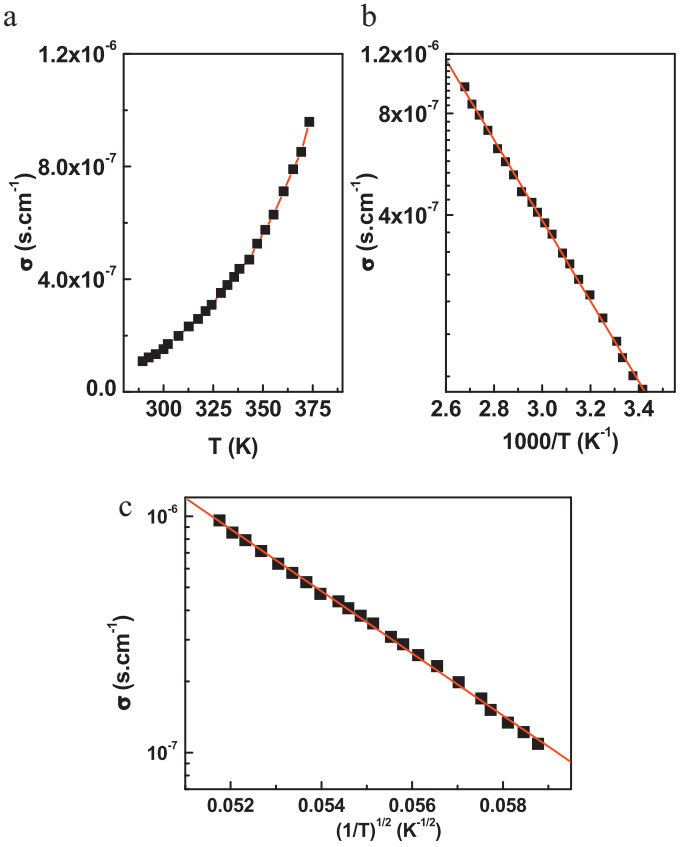

Fig. 8. (a) Temperature dependence of dark electrical conductivity, σ_{DC}, and (b) semilog plot of, σ_{DC} vs. 1000/T for SCC film. (c) Semilog plot of dark electrical conductivity, σ_{DC} vs. $1/T^{1/2}$ for SCC film (according to 1D-VRH).

in a Coulomb gap [33]. In the case of organic semiconductors and in highly disordered materials the tight band approximation is replaced by their extended states. The conduction in the extended state is analogue to the crystalline material and in the localized states due to hopping process. The VRH model has been extensively applied to various amorphous semiconductors over the last few decades, and recently has also been applied with a varying degree of success to conducting polymers [34]. Recently, Altındal et al. [35] have shown the applicability of Mott's VRH model in 3-dimensions for spin coated phthalocyanine films. One-dimensional variable range hopping (VRH) was successful for the thermally evaporated carbazol [30], several polymers [36] and nanocrystalline oxazine films [37].

According to the VRH model, the temperature dependence of conductivity is given by [37]

$$\sigma_{DC}(T) = \sigma_0 \exp\left(-\frac{T_0}{T}\right)^{1/(n+1)}, \quad (4)$$

where the parameter n corresponds to one, two and three dimensions (n = 1, 2, 3), T_0, is associated with the degree of localization of the electronic wave function or hopping barrier. As a representative result, we have plotted $\log \sigma_{DC}$ as a function of $T^{-1/2}$, shown in Fig. 8(c). The resultant best fit to the experimental data is in agreement with one-dimensional variable range hopping (1D-VRH) model proposed by Mott and Davis [32], and published by other authors [38–41].

The value of Mott characteristic temperature T_0 can be calculated from the slope of Fig. 8(c) and listed in Table 3. The hopping

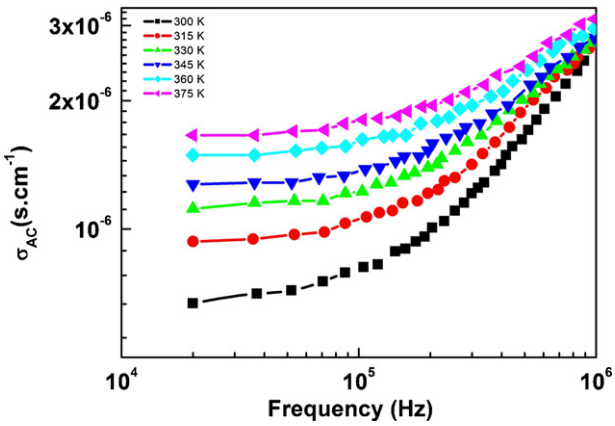

Fig. 9. Semilog plot of dark AC conductivity, σ_{AC} vs. frequency for SCC film at different temperatures.

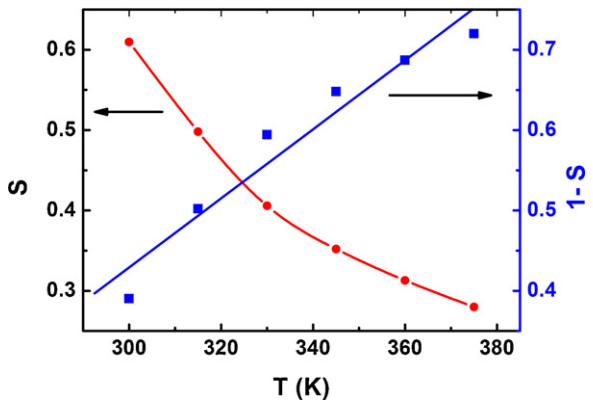

Fig. 10. Temperature dependence of the frequency exponent, *s*, for SCC film.

energy ΔW and the average hopping distance $\langle R\rangle$ are given by the following equations [30].

$$\Delta W = \frac{k}{2}(T_0 T)^{1/2} \tag{5}$$

$$\langle R\rangle = \frac{\psi}{4}\left(\frac{T_0}{T}\right)^{1/2}, \tag{6}$$

where ψ is the wavefunction decay length (localization length). Taking the value of 0.5 nm for ψ [30], the values of hopping energy and the average hopping distance are determined and collected in Table 3.

In the hopping model the charge carriers hop from one localized state to another. When it falls on a defect state, it is virtually trapped in that state due to the potential well-created due to the atomic polarization. Thus, the activation energy in the hopping process is to excite charge carriers from one localized state to the next [30,35]. The obtained parameters for SCC film are compared with other published for one-dimensional variable range hopping (VRH) of different materials and listed in Table 3.

The formation of grain boundaries in the nanostructural SCC can also affect the electrical conductivity. The charged states at the grain boundary create depleted regions and the potential barriers that provide a resistance for the passage of carriers. The grain-boundary barrier models have been successfully used to explain most of the electrical properties in many polycrystalline materials. The structure of grain boundaries can be assumed to have the same structure as that of intrinsic trapping defect states and they are formed in the film due to defects formed during film preparation. In such cases the resistivity is due to the depleted space charge regions and the grain boundary potential barriers that impede thermionic emission of charge carriers into the grains [30].

3.5. AC electrical characteristics of SCC film

Fig. 9 shows the frequency dependence of the AC conductivity, $\sigma_{AC}(\omega)$ in semilogarithmic plot, of SCC film at different temperatures in the range 300–375 K. It is evident that $\sigma_{AC}(\omega)$ is both frequency and temperature dependent and increases with increasing frequency and temperature. However, the influence of temperature is more pronounced in the low frequency range, while at the high frequencies edge the values of $\sigma_{AC}(\omega)$ display proximity. At low frequencies, the applied electric field forces the charge carriers to drift over large distances. As the temperature is increased, a tendency to retain almost constant values is recorded. When frequency is raised, the mean displacement of the charge carriers is reduced and the real part of conductivity, after reaching a certain critical frequency f_c, follows the law $\sigma_{AC}(\omega) \sim \omega^s$ with $0 \le s \le 1$ characterizing hopping conduction [42,43]. The critical frequency f_c has been found to be little dependent on temperature [44–46]. The dispersion of $\sigma_{AC}(\omega)$ with frequency is a common characteristic in heterogeneous, disordered and nanostructural solids [42,47–49]. In general, at a constant temperature $\sigma_{AC}(\omega)$ can be expressed as [49]

$$\sigma_{AC}(\omega) = \sigma_{DC} + A(\omega)^s \tag{7}$$

where σ_{AC} is the AC conductivity, ω is the angular frequency, σ_{DC} is the $\omega \to 0$ limiting value of $\sigma_{AC}(\omega)$, A is the proportionality constant and s is the index which is characteristic of the type of conduction mechanism/relaxation mechanism dominant in amorphous materials [9,27]. The variation of exponent s with temperature gives information about the conduction mechanism involved. The value of s is less than unity for all SCC samples. An increase in $\sigma_{AC}(\omega)$ with frequency and temperature indicate that there may be charge carriers, which are transported by hopping through the defect sites along the film structure [50].

Values of the frequency exponent s were calculated from the slopes of these lines in the high frequency range, using a power law (Eq. (7)) at different temperatures. The variation of s with temperature is shown in Fig. 10, in which it decreases with increasing temperature. To decipher the conduction behavior with respect to both frequency and temperature, different theoretical models have been proposed to correlate the conduction mechanism of $\sigma_{AC}(\omega)$ with $s(T)$ behavior. Theories proposed for AC conduction in amorphous or nanostructural semiconductors [51] have mostly assumed that carrier motion occurs through quantum mechanical tunneling, QMT [52–54].

In the quantum mechanical tunneling (QMT) model [55,56], the exponent s is almost equal to 0.8 and increases slightly with increasing temperature or is independent of temperature. Therefore, the QMT model is not applicable to the obtained results. But in the non-overlapping small polaron tunneling (NSPT) model, the exponent s is temperature dependent, increased with increasing temperature. Therefore, the NSPT model also is not applicable to the obtained results [57]. In the overlapping-large polaron tunneling (OLPT) model [58], the exponent s is both temperature and frequency dependent. Also, s decreases with increasing temperature to a minimum value at a certain temperature then continues to increase with increasing temperature. Therefore, the OLPT model is also not applicable to the obtained results. When applying the correlated barrier hopping (CBH) model, values of s decrease with increasing temperatures. This is in good agreement with the obtained results, as shown in Fig. 10. Accordingly, the correlated barrier hopping (CBH) is the most predominant hopping mechanism in SCC film and the frequency dependence of σ_{AC} can be explained in terms of this model. Correlated barrier hopping (CBH) model was applied for

various organic compounds [59–61]. In the CBH model [60], carrier motion occurs by means of hopping over the Coulomb barrier separating two defect centers and the exponent s was found to obey the equation:

$$S = 1 - \frac{6kT}{W_m - kT\ \ln(1/\omega\tau_0)} \quad (8)$$

where W_m is the maximum barrier height for hopping at infinite separation, i.e., the binding energy of the carrier in its localized sites and τ_0 is a characteristic relaxation time which is in the order of an atom vibrational period $\tau_0 = 10^{-13}$ s [62]. For which, to a first approximation reduces to the simple expression (for large values of W_m/kT), the exponent s becomes [62]:

$$S = 1 - \frac{6kT}{W_m} \quad (9)$$

The energy W_m is equal to the bandgap (E_g) of the material for bipolaron hopping [63]. For the case of single-polaron transport, the value of W_m by the CBH mechanism is typically one quarter that for bipolaron motion, and the conductivity would be correspondingly higher [63]. By determining the slope from the dependency of $(1-s)$ versus T curve (Fig. 10) and using Eq. (9) the potential barrier (W_m) was found to be 0.192 eV. This is not consistent with the activation energy estimated from the optical band gap energy of the nanostructured SCC thin films. Experimentally the energy W_m can take any value equal or less than energy gap of the film material depending on film's morphological structure, average grain size, defect distribution and density, phase content of the sample (mono- or multi-phases), and crystallographic orientation state of the film [63–65]. These factors did not enter into the CBH model derived originally for uniform homogeneous non-crystalline insulators. Therefore, experimentally s can take any value less than unity.

Fig. 11(a) shows the semilogarithmic plot of σ_{AC} as a function of the reciprocal temperature in the investigated temperature range at different frequencies for the SCC film. It is clear that σ_{AC} increases linearly with the reciprocal of the absolute temperature. This dependence of σ_{AC} on temperature suggests that the AC conductivity is a thermally activated process and it can be analyzed according to the well-known Arrhenius equation.

The AC activation energy of conduction was calculated at different frequencies from the slopes of the obtained straight lines of Fig. 11(a) at different frequencies. The frequency dependence of $\Delta E(\omega)$ for SCC film is shown in Fig. 11(b). Clearly, values of $\Delta E(\omega)$ decrease with increasing applied frequency. Such behavior can be attributed to the contribution of the applied frequency to the conduction mechanism, which confirms the hopping conduction to be the dominant mechanism [60]. The increment of the applied field frequency enhances the electronic jumps between localized states; hence the electrical activation energy decreases with increasing of the applied frequency [66].

3.6. Dielectric characteristics of SCC film

The frequency and temperature dependences of the real part of dielectric constant, ε_1 in the temperature range 300–375 K at different applied frequencies in the range 20 kHz–1 MHz is shown in Fig. 12(a) and (b). A comparative study of these results indicates that the value of ε_1 increases with the increase of temperature and decrease with the increase of frequency. The rate of the increase by rising temperature is faster at higher temperatures and the rate of decrease by increasing frequency is faster at lower frequencies. This behavior has been also observed in other organic films [59,60,67–70]. It is observed that the dielectric constant increases with the increase in temperature due to the charge carriers, which in most cases cannot orient themselves with respect to the direction

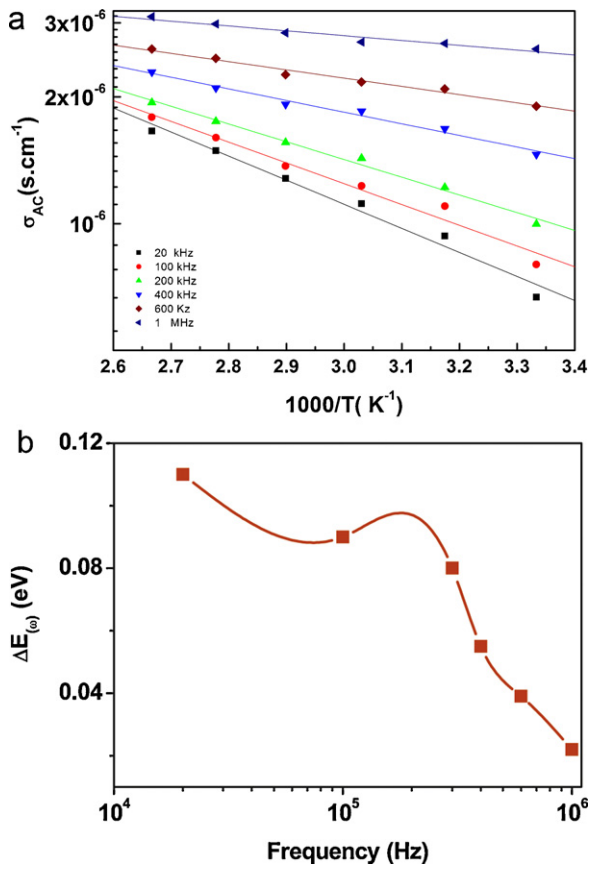

Fig. 11. (a) Semilog plot of AC conductivity, σ_{AC} vs. $1000/T$ at different frequencies for SCC film. (b) Frequency dependence of the activation energy, ΔE for SCC film.

of the applied field, since they possess a weak contribution to the polarization. As the temperature increases, the bound charge carriers get enough thermal excitation energy, which are able to respond the change in the external field more easily. This in turn enhances their contribution to the polarization leading to an increase of the dielectric constant ε_1 of the sample [59,60]. At constant temperature in slowly varying fields at low frequency, the dipoles align themselves along the field direction and fully contribute to the total polarization. As the frequency is increased, the variation in the field

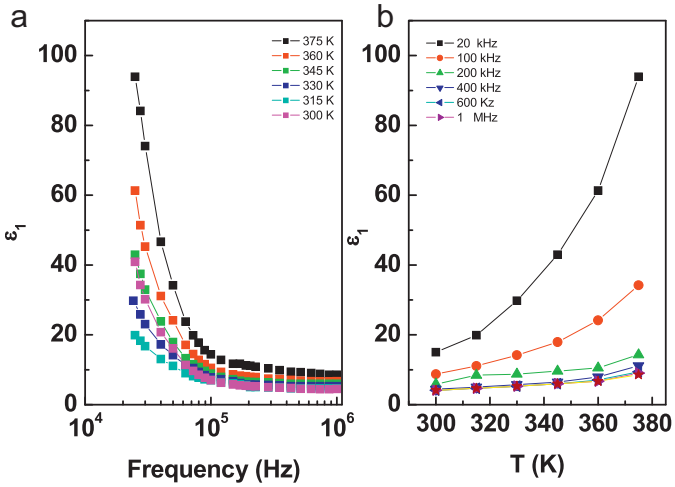

Fig. 12. (a) Semilog plot of real part of dielectric constant, ε_1 vs. frequency and (b) real part of dielectric constant, ε_1 vs. temperature, T for SCC films.

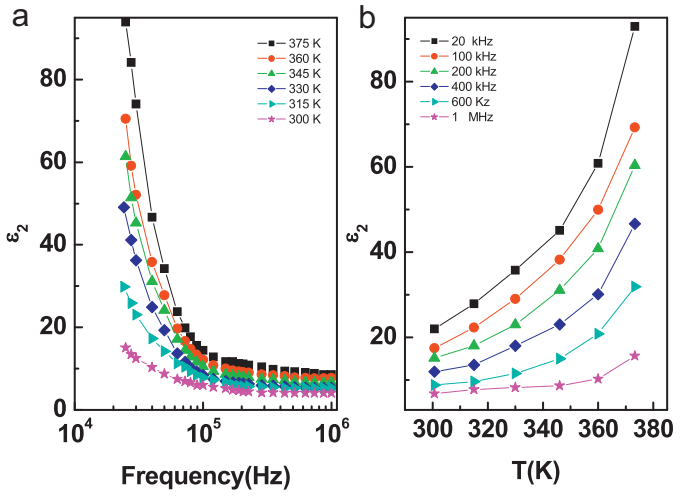

Fig. 13. (a) Semilog plot of imaginary part of dielectric constant, ε_2 vs. frequency and (b) real part of imaginary part of dielectric constant, ε_2 vs. temperature, T for SCC films.

becomes too rapid for the molecular dipoles to follow, so that their contribution to the polarization becomes less.

The variation in the dielectric loss ε_2 as a function of temperature and frequency is similar to that for the dielectric constant ε_1, this is clear from Fig. 13(a) and (b). Fig. 13(a) shows that ε_2 is a low temperature dependent at low temperature range, and then it increases with increasing temperature. On the other hand, Fig. 13(b) shows that ε_2 decreases with increasing frequency up to about 500 kHz, above this value it seems to be low frequency dependent. The rapid increment of ε_2 at relatively high temperatures can be explained in terms of the conduction losses [71]. The conduction losses usually increase with the increment in the σ_{AC} towards high temperatures.

The frequency dependence of $\varepsilon_2(\omega)$ is represented as $\log \varepsilon_2(\omega)$ versus $\log \omega$, as given in Fig. 14(a) for the investigated SCC film. It is clear that the obtained curves are fitted to two linear straight lines depending on the frequency at various temperatures. According to Guintini et al. [39], $\varepsilon_2(\omega)$ at a particular frequency in the temperature range where dielectric dispersion follow the relation [39]:

$$\varepsilon_2(\omega) \propto \omega^{m(T)}, \tag{10}$$

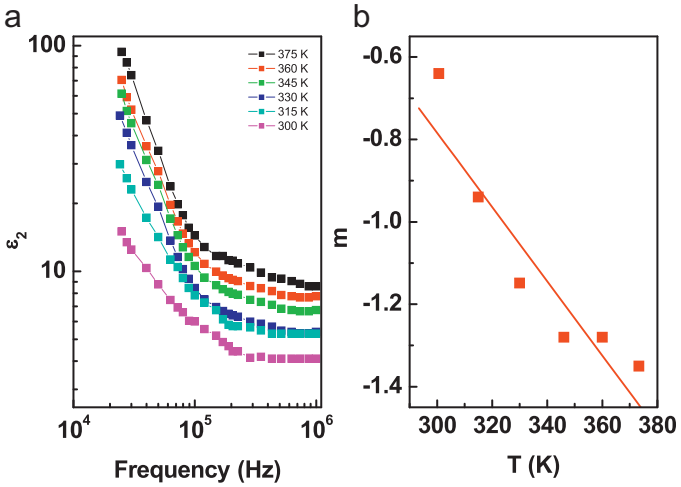

Fig. 14. (a) Logarithmic plot of ε_2 vs. frequency. (b) Temperature dependence of the exponent m.

where m is the power exponent dependent on temperature. The power $m(T)$ of this equation was calculated from the negative slopes of the obtained straight lines of Fig. 14(a) at low frequency range at different temperatures. The variation of the obtained values m with temperature is shown in Fig. 14(b). The results illustrate that m decreases with increasing temperature. Such a dependence of $m(T)$ on temperature satisfies the following relation [39].

$$m = -\frac{4kT}{W_M} \tag{11}$$

From the above equation, the power, m, should be negative and decreases with increasing temperature showing a linear fit behavior, which is confirmed in Fig. 14(b). The value of W_M was estimated as 0.038 eV for SCC thin film. This value is comparable with those obtained for organic materials [13,36] by this model. The disagreement between the obtained values of W_m and W_M may be due to the approximation, that made by ignoring the frequency term, which may be resulted in relatively high value of W_m, while the calculation of W_M takes the frequency into account [70].

3.7. Absorption and energy gap determination

The absorption spectrum of SCC thin film is shown in Fig. 15(a). They have very strong absorption bands in the visible region of the spectrum. The well-known band of the SCC molecule, namely Q-band appears in the region between 470 and 670 nm. As observed, SCC film shows two peaks. The higher wavelength side peak has a lower intensity than the observed at the lower wavelength side. The distinct characterized peaks for SCC in the visible region (Q-band) at 470 and 640 nm have generally been interpreted in terms of the first and the second π–π^* excitation between bonding and antibonding molecular orbitals [11,19]. It can also be noticed that this band shows the characteristic splitting (Davydov splitting) in

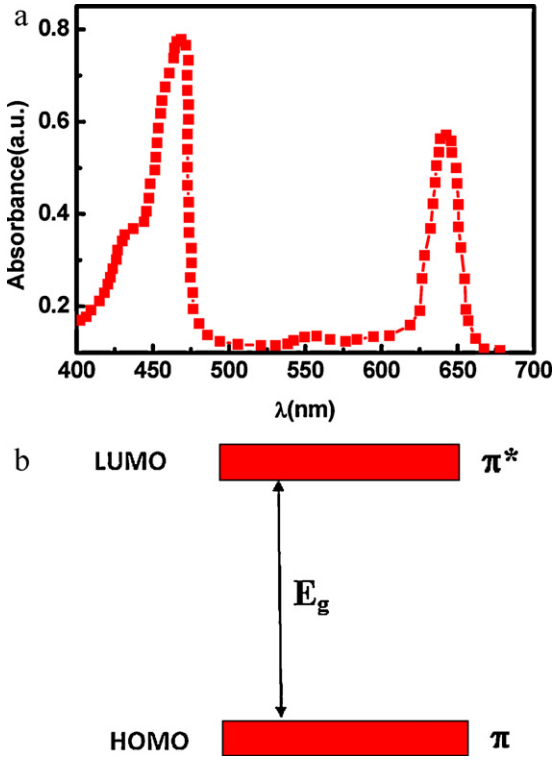

Fig. 15. (a) Spectral dependence of absorbance of SCC film in the range 400–700 nm. (b) Simplified schematic diagram of the energy gap separation between the highest occupied molecular orbital (HOMO) and the lowest unoccupied molecular orbital (LUMO).

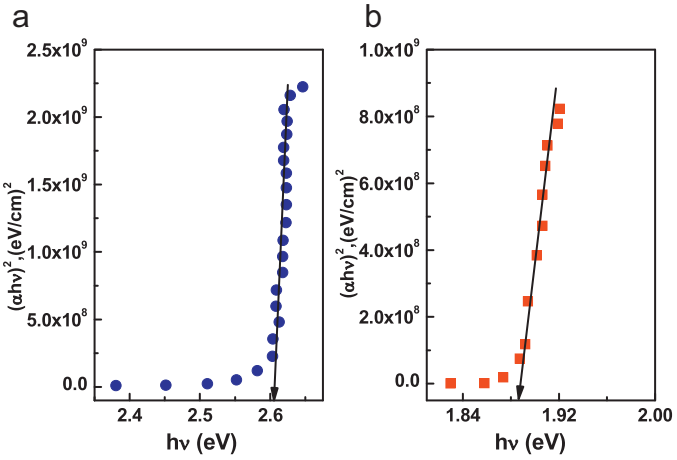

Fig. 16. Plot of $(\alpha h\nu)^2$ vs. $h\nu$ (a) first region and (b) second region of SCC film.

the high characteristic peak which has a value of 0.23 eV for SCC in agreement with the other organic molecules [11,19]. According to Davydov's theory the amount of splitting is a measure of the interaction energy between molecules having different site symmetries. The bands split into as many components as there are non-transitionally equivalent molecules in the unit cell. Thus, the observed weak splitting confirms the out of plane bonding in SCC. The simplified schematic diagram of the energy gap separation between the highest occupied molecular orbital (HOMO) and the lower unoccupied molecular orbital (LUMO) is shown in Fig. 15(b).

The applicability of using the band theory to describe the electronic transition in organic systems was suggested by various authors [26,72–75]. They studied HOMO–LUMO gap of some organic semiconductors and suggested that a transition of electron in an organic molecule is promoted from the highest occupied molecular orbital HOMO to the lowest unoccupied molecular orbital LUMO. Thus, for a molecular crystal the valence band is formed by the combination of the highest occupied molecular orbital (HOMO; π-orbital) whereas the lowest unoccupied molecular orbital (LUMO; π*-orbitals) contribute to the conduction band. These bands are separated by the band gap (E_g).

To obtain information about direct or indirect inter-band transitions, the optical band gap was determined from the analysis of the spectral dependence of the absorption near fundamental absorption edges within the framework of one electron theory [48,49]. This theory can be used to analyze the absorption edge data of molecular solids such as phthalocyanine derivative [74,75]. The dependence of $(\alpha h\nu)^r$ on photon energy $h\nu$ was plotted for different values of r and the best fit was obtained for $r = 2$. The absorption coefficient, α, is well-described by the relation [74,75].

$$(\alpha h\nu)^2 = A(h\nu - E_g) \tag{12}$$

where E_g is the value of the optical band gap and the factor A depends on the transition probability which can be assumed to be constant within the optical frequency range. Plots of $(\alpha h\nu)^2$ vs. $(h\nu)$ near the absorption edge of the Q and B bands for the SCC are shown in Fig. 16(a) and (b). The extrapolation of the straight line graphs to zero absorption gives the values of the onset and transport energy gap. It is worth to mention that the transport gap "HOMO–LOMO gap", E_t, is the minimum energy formation of a separated, uncorrelated free electron and hole that associated with the transport of single particles in the solid. On the other hand, the optical gap, E_{opt} corresponds to the onset of optical absorption and formation of a bound electron–hole pair or exciton. For most organic molecules, the calculated transport gap E_t is larger than the calculated optical band gap, E_{opt} by a significant amount corresponding to the binding

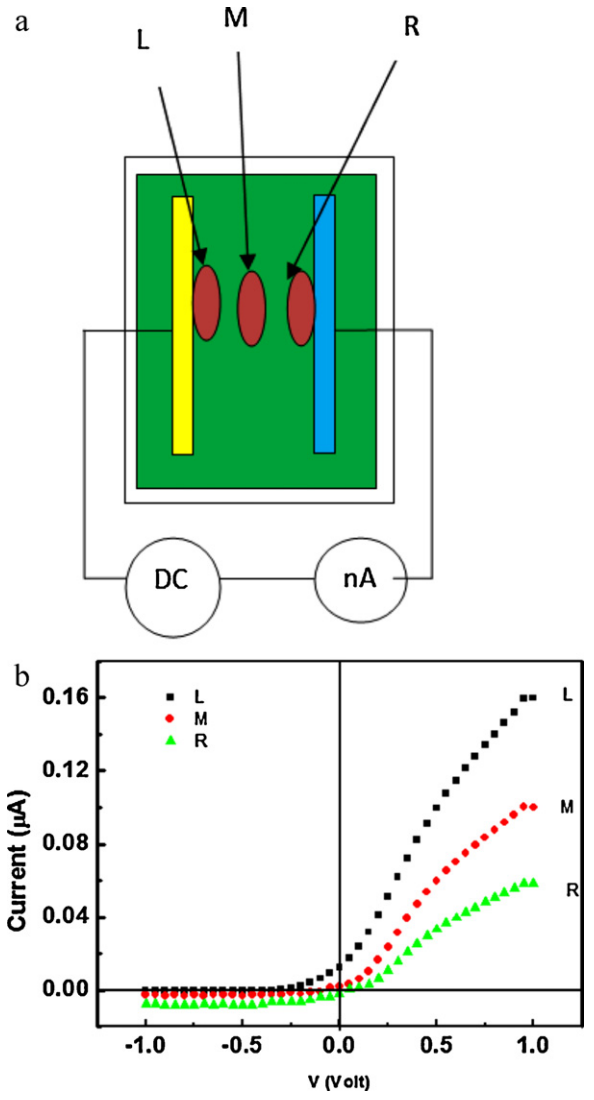

Fig. 17. (a) Schematic diagram of the device. L, M and R are three different positions of laser spot illumination for the device. (b) Current–voltage (I–V) characteristics of SCC device at different positions (L, M and R are three different positions of laser spot illumination).

energy of the exciton, E_B. It may be noted that the exciton binding energy mainly depends on the dielectric constant of the material, molecular size and charge distribution on the molecule [76]. The binding energy of the exciton for most organic molecules lies in the range $E_B = 0.5$–1.7 eV [76,77]. The obtained values of E_{opt} and E_t are 1.88 and 2.6 eV, respectively. Accordingly, the corresponding exciton binding energy, $E_B = E_t - E_{opt} = 0.72$ eV, is in agreement with other molecular solids [76]. The high value of the exciton binding energy may be attributed to the molecular nature of organic solids and low dielectric constant for most organic molecules [77].

3.8. Photodiode application of SCC film

Position dependent of SCC thin film photo-detector has been studied by using laser diode source. Fig. 17(a) shows a schematic diagram of the device. L corresponds to illumination on the left electrode/film interface, R corresponds to illumination on the right electrode/film interface, and M corresponds to the middle position of the film. Fig. 17(b) shows the photocurrent with different laser spot positions. The photocurrent either increases, decreases or remains almost zero, depending on the position of the

laser spot with respect to the electrodes. In detail, the *J–V* curves for position M and in dark lie on top of the one another and pass directly through the origin. Whereas, when the light illuminated at position L and R, the *J–V* curve is shifted above or below the origin, respectively.

A large enhancement of photocurrent as well as photo-voltage at the interface indicates that there is an existence of locally generated electric field at the metal/SCC film interface. This mechanism of the local electric field generation was explained using Schottky barrier (SB) model. When red spot is illuminated on the left electrode/SCC film interface, excitons are generated and dissociated into free charge carriers at the interface. Since SCC thin film has a lot of localized states, it will also help in dissociation of excitons into free carriers. Some of the free carriers (holes) might have sufficient energy to overcome the Schottky barrier and enter into the metal electrode leaving the electron in the film. This causes a hole–electron separation at the interface creating a positive photovoltage.

4. Conclusions

The nanocrystalline structure of the SCC film prepared by dip coating was confirmed by using SEM, PSA and XRD. The thermal stability was checked by TGA in the studied temperature range. The DC electrical conductivity studies were carried out and it was found that the conduction is due to variable range hopping (VRH) mechanism. The AC conductivity of SCC is found to be proportional to $\omega^{s(T)}$ and the temperature dependence of both AC conductivity and the frequency exponent are reasonably well-interpreted in the context of the (CBH) model. The dielectric relaxation mechanism was explained based on the temperature dependent of both $\varepsilon_1(\omega)$ and $\varepsilon_2(\omega)$ at different frequencies. The optical properties of SCC thin films show that, two absorption bands were observed, namely, the Soret (B-band) and the Q-band. The transport phenomena and the optical band gap as well as the exciton binding energy are found to be 2.6, 1.88 and 0.72 eV, respectively. The position dependent SCC thin film photo-detector was also detected.

Acknowledgement

One of the authors (A.A.M. Farag) would like to acknowledge Dr. H.A. Hussainy (Pharmaceutical Science Department, National Research Center, Cairo, Egypt) for providing the powder of SCC.

References

[1] L. Leontie, R. Dana, Scripta Mater. 54 (2006) 175.
[2] O. Gullu, A. Turut, J. Alloys Compd. 509 (2011) 571.
[3] S. Rasouli, S.J. Moeen, J. Alloys Compd. 509 (2011) 1915.
[4] A. Natalia Azarova, J.W. Owen, C.A. McLellan, M.A. Grimminger, E.K. Chapman, J.E. Anthony, O.D. Jurchescu, Org. Electron. 11 (2010) 1960.
[5] S. Nenon, D. Kanehira, N. Yoshimoto, F. Fages, C. Videlot-Ackermann, Thin Solid Films 518 (2010) 5593.
[6] D. Gupta, Y. Hong, Org. Electron. 11 (2010) 127.
[7] http://en.wikipedia.org/wiki/Chlorophyllin.
[8] P. Stallinga, H.L. Gomes, M. Murgia, K. Mullen, Org. Electron. 3 (2002) 43.
[9] Y. Yun, C.r. Pearson, D.H. Cadd, R.L. Thompson, M.C. Petty, Org. Electron. 10 (2009) 1596.
[10] M. Gratzel, Pure Appl. Chem. 73 (2001) 459.
[11] A.A.M. Farag, Spectrochim. Acta A 65 (2006) 667.
[12] A.A.M. Farag, Appl. Surf. Sci. 255 (2009) 4938.
[13] M. Abdel Rafea, A.A.M. Farag, N. Roushdy, J. Alloys Compd. 485 (2009) 660.
[14] M. Gazizov, V. Teleshov, V. Zakharov, R. Kaibyshev, J. Alloys Compd. 509 (2011) 9497.
[15] Y.M. Sun, J. Alloys Compd. 509 (2011) 499.
[16] R. Seoudi, G.S. El-Bahy, Z.A. El Sayed, J. Mol. Struct. 753 (2005) 119.
[17] R. Shirley, The CRYSFIRE System for Automatic Powder Indexing: User's Manual, The Lattice Press, Guildford, Surrey, England, 2000.
[18] J. Laugier, B. Bochu, LMGP-Suite Suite of Programs for the Interpretation of X-ray Experiments, ENSP/Laboratoire des Materiaux et du Genie Physique, BP46.38042, Saint Martin d'Heres, France, 2000.
[19] M.M. El-Nahass, H.M. Zeyada, K.F. Abd-El-Rahman, A.A.M. Farag, A.A.A. Darwish, Spectrochim. Acta A 69 (2008) 205.
[20] J.R. Dyer, Applications of Absorption Spectroscopy of Organic Compounds, Prentice-Hall of India (P), New Delhi, 1987.
[21] T.M. Kolev, D.Y. Kancheva, B.A. Stamboliyska, Spectrochim. Acta A 59 (2003) 3325.
[22] M.M. El-Nahass, H.M. Zeyada, M.S. Aziz, M.M. Makhlouf, Spectrochim. Acta A 62 (2005) 11.
[23] H. Oshio, T. Ama, T. Wadanabe, J. Kincid, K. Nakamoto, Spectrochim. Acta A 40 (1984) 863.
[24] A. Ahmed, R.A. Collins, Phys. Stat. Sol. A 123 (1991) 201.
[25] A. Ahmed, R.A. Collins, J. Phys. D: Appl. Phys. 24 (1991) 1894.
[26] A.A.M. Farag, Opt. Laser Technol. 39 (2007) 728.
[27] H.J. Li, X.Y. Qin, Y. Liu, D. Li, J.L. Hu, J. Alloys Compd. 509 (2011) 3677.
[28] X. Xiong, Z. Liu, J. Ouyang, X. Xia, J. Xiang, X. Liu, J. Alloys Compd. 509 (2011) 8392.
[29] X. Tong, W. Zhu, Q. Wu, X. Qian, Z. Liu, W. Yan, J. Gong, J. Alloys Compd. 509 (2011) 7768.
[30] K. Pisharady Sreejith, C.S. Menon, C. Sudarsanakumar, Vacuum 82 (2008) 1291.
[31] Z.H. Wang, E.M. Scherr, A.G. MacDiarmid, E.J. Epstein, Phys. Rev. B 45 (1992) 4190.
[32] N.F. Mott, E.A. Davis, Electronic Processes in Non-crystalline Materials, Calerendon, Oxford, 1979.
[33] E.A. Efros, B.I. Shkloviskii, J. Phys. C: Solid State Phys. 8 (1975) L49.
[34] P. Dutta, S.K. De, Synth. Met. 139 (2003) 201.
[35] A. Altındal, S. Abdurrahmanoglu, M. Bulut, O. Bekaroglu, Synth. Met. 150 (2005) 181.
[36] Y. Koval, I. Lazareva, P. Muller, Synth. Met. 161 (2011) 528.
[37] A.A.M. Farag, F.S. Terra, G.M. Mahmoud, Synthetic Metals 160 (2010) 743.
[38] J. Huang, M. Wan, Solid State Commun. 108 (1998) 255.
[39] J.C. Guintini, J.V. Zanchetta, D. Jullien, R. Eholie, P. Houenou, J. Non-cryst. Solids 45 (1981) 57.
[40] G.M. Spinks, S.J. Kim, Sens. Actuators B 134 (2008) 122.
[41] L. Zhang, M. Wan, Thin Solid Films 477 (2005) 24.
[42] J.C. Dyre, T.B. Shrder, Rev. Mod. Phys. 72 (2000) 873.
[43] H. Bottger, U.V. Bryskin, Hopping Conduction in Solids, Verlag Akademie, Berlin, 1985.
[44] G.M. Tsangaris, G.C. Psarras, E. Manolakaki, Adv. Comp. Lett. 8 (1999) 25.
[45] G.C. Psarras, E. Manolakaki, G.M. Tsangaris, Compos. A: Appl. Sci. Manufact. 33 (2002) 375.
[46] A. Sharma, N. Mehta, A. Kumar, J. Alloys Compd. 509 (2011) 3468.
[47] G.C. Psarras, E. Manolakaki, G.M. Tsangaris, Compos. A: Appl. Sci. Manufact. 34 (2003) 1187.
[48] J.C. Dyre, T.B. Schrder, Phys. Stat. Sol. B 230 (2002) 5.
[49] E. Abd El-Wahabb, M.M. Abd El-Aziz, E.R. Sharaf, M.A. Afifi, J. Alloys Compd. 509 (2011) 8595.
[50] A.K. Jonscher, Thin Solid Films 1 (1967) 213.
[51] P. Extance, S.R. Elliott, E.A. Davis, Phys. Rev. B 32 (1985) 8148.
[52] http://users.jyu.fi/~mmannine/BasicNanoSci/QTnanoIM1.pdf.
[53] E.F. Redish, M.C. Wittmann, R. Steinberg, AAPT Summer Meeting, Talk CF14, Summer, 2000.
[54] B.S. Ambrose, P.R.L. Heron, S. Vokos, L.C. McDermott, Am. J. Phys. 67 (1999) 891.
[55] A. Ghosh, Phys. Rev. B 41 (1990) 1479.
[56] M. Pollak, Phil. Mag. 23 (1971) 519.
[57] A. Ghosh, Phys. Rev. B 42 (1990) 5665.
[58] A.R. Long, Adv. Phys. 31 (1982) 553.
[59] A. Tataroglu, I. Yucedag, S. Altindal, Microelectron. Eng. 85 (2008) 1518.
[60] V. Chithambaram, S. Jerome Das, S. Krishnan, J. Alloys Compd. 509 (2011) 4543.
[61] S. Senthilarasu, R. Sathyamoorthy, J.A. Ascencio, S.H. Lee, Y.B. Hann, J. Appl. Phys. 101 (2007) 034111.
[62] K.H. Mahmoud, F.M. Abdel-Rahim, K. Atef, Y.B. Saddeek, Curr. Appl. Phys. 11 (2011) 55.
[63] A.A. Dakhel, Thin Solid Films 496 (2006) 353.
[64] R.H. Chen, R.Y. Chang, S.C. Shern, J. Phys. Chem. Solids 63 (2002) 2069.
[65] R.H. Chen, S.C. Shern, T. Fukami, J. Phys. Chem. Solids 63 (2002) 203.
[66] N.F. Mott, E.A. Davis, Electronic Processes in Non-crystalline Materials, Clarendon Press, Oxford, 1971.
[67] I. Dokme, S. Altindal, T. Tunc, I. Uslu, Microelectron. Reliab. 50 (2010) 39.
[68] H. Sahni, S.K. Gupta, A.J. Mehra, Appl. Polym. Sci. 20 (2011) 390.
[69] M.M. El-Nahass, A.F. El-Deeb, F. Abd-El-Salam, Org. Electron. 7 (2006) 261.
[70] E.M. El-Menyawy, H.M. Zeyada, M.M. El-Nahass, Solid State Sci. 12 (2010) 2182.
[71] U. Akgul, Z. Ergin, M. Sekerci, Y. Atici, Vacuum 82 (2008) 340.
[72] S. Ambily, C.S. Menon, Thin Solid Films 347 (1999) 284.
[73] B. Bialek, I.G. Kim, J.I. Lee, Synth. Met. 129 (2002) 151.
[74] M.M. El-Nahass, A.A.M. Farag, K.F. Abd El-Rahman, A.A.A. Darwish, Opt. Laser Technol. 37 (2005) 513.
[75] M.M. El-Nahass, T.E. Youssef, J. Alloys Compd. 503 (2011) 86.
[76] P.K. Nayak, N. Periasamy, Org. Electron. 10 (2009) 1396.
[77] D. Cahen, A. Kahn, E. Umbach, Mater. Today 8 (2005) 32.